Journal of Catalysis 381 (2020) 175–185

Contents lists available at ScienceDirect

Journal of Catalysis

journal homepage: www.elsevier.com/locate/jcat

The synergistic effect of proton intercalation and electron transfer via electro-activated molybdenum disulfide/graphite felt toward hydrogen evolution reaction

Danlian Huang *, Lei Lei, Rui Deng, Sha Chen, Zhihao Li, Chen Zhang, Wenjun Wang, KunKun Wang

College of Environmental Science and Engineering, Hunan University, Changsha, Hunan 410082, China
Key Laboratory of Environmental Biology and Pollution Control (Hunan University), Ministry of Education, Changsha, Hunan 410082, China

ARTICLE INFO

Article history:
Received 7 August 2019
Revised 23 October 2019
Accepted 2 November 2019

Keywords:
Hydrogen evolution
MoS_2/GF
Electrochemical activation
Proton intercalation
DFT calculations

ABSTRACT

Molybdenum disulfide (MoS_2) possesses promising prospects of application in electrocatalytic hydrogen evolution. However, the MoS_2 prepared by traditional hydrothermal method is usually 2H (hexagonal) semiconducting state with limited active sites and unsatisfied conductivity, hindering the improvement of hydrogen evolution efficiency. Herein, the MoS_2 nanoflowers are in-situ grown successfully on graphite felt (GF) by hydrothermal method, and a simple and effective electrochemical activation is proposed to enhance the hydrogen evolution activity of the composite. The electrical activation in acidic medium guides the intercalation of protons between MoS_2 and GF, and the increased interlayer spacing between MoS_2 is conducive to the adsorption and release of hydrogen. The synergistic effect between MoS_2 and GF is enhanced, resulting in accelerated electron transfer through S sites in MoS_2 and oxygen-containing functional group in GF. The experimental results and density functional theory (DFT) computations demonstrate that the electrical activated catalyst possesses excellent electrocatalytic activity and long-term operation stability (Tafel slope is 48 mV dec^{-1}, the overpotential is 82 mV at current density of −10 mA cm^{-2}). Our research confirms the electrochemical activation is a simple technique for enhancing the hydrogen evolution efficiency of MoS_2/GF composite as well as other transition metal chalcogenides and carbon materials.

1. Introduction

With the increasing craving for clean energy production, hydrogen (H_2), as a clean and renewable energy carrier, has attracted more and more attention. Electrocatalytic decomposition of water is the cheapest and most efficient strategy to transform electricity comes from other renewable sources in the form of H_2 [1,2]. For this purpose, it is indispensable to evolve an active and durable electrocatalyst to minimize the kinetic overpotential required for H_2 evolution reaction (HER) and ultimately ameliorate its efficiency. Pt-based materials have been always recognized as the most promising HER electrocatalysts, yet, their high costs and extreme scarcity are also daunting [1,3]. Thus, it is of great significance to develop inexpensive, profuse as well as high-efficiency electrocatalysts for the water splitting.

In the past ten years, molybdenum disulfide (MoS_2), as a prolific, highly active and electrochemical stable material, has been proved to be a promising electrocatalytic H_2 evolution material in both calculations and experiments [1,4,5]. MoS_2 possesses two-dimensional (2D) layered structure similar to graphene, which mainly exists in two phase states, i.e. 2H (hexagonal) phase (2H-MoS_2) and 1T (trigonal) phase (1T-MoS_2), and most of the prepared MoS_2 are 2H phase. The HER activity of 2H-MoS_2 is widely considered to be derived from the edges of the layered structure rather than from basal planes due to the affinity between H atoms and marginal unsaturated S atoms, and the basal planes are considered chemically inert [5–7]. However, the inherent overlap between Van der Waals forces in the MoS_2 layer greatly limits the number of exposed active centers [8]. Inspired by this understanding, morphological and structural engineering design are feasible strategies for enhancing the catalytic performance of MoS_2 without sacrificing the properties of MoS_2 crystals [6,9]. Advanced strategies of synthesizing nanostructured MoS_2 with more exposed edge sites to strengthen electrocatalytic HER have been studied, representative researches, such as nanoscale MoS_2 hollow spheres [10], defective nanosheets [11], edges exposed porous membrane [12], double coiled spiral structure [13], perpendicular film [14], amorphous film [15], and nanoflowers, etc. [16]. Among these

* Corresponding author at: College of Environmental Science and Engineering, Hunan University, Changsha, Hunan 410082, China.
E-mail address: huangdanlian@hnu.edu.cn (D. Huang).

https://doi.org/10.1016/j.jcat.2019.11.003
0021-9517/

MoS_2 with abundant exposed edges, MoS_2 nanoflowers seem to be the most widely studied structures. On the one hand, the floral structure allows a large number of edges to exist stably; on the other hand, MoS_2 nanoflowers are easily prepared in large quantities via simple hydrothermal methods [17,18].

Regrettably, due to the unsatisfactory electron transport ability between particles, the conductivity of MoS_2 in nanostructured materials is generally relatively poor, leading to the decrease of HER activity [1,19]. In response to this flaw, studies have been devoted to combining MoS_2 with some carbon materials, such as glassy carbon [20], graphite paper [21] or graphene [22] to provide conductive channels for semiconductor MoS_2 nanosheets, thereby improving the properties of HER [8]. Howbeit, the performance improvement is not obvious unless further interlaminar expansion and ions intercalation process are adopted. In addition, during the cycling process, the volume of MoS_2 crystal changes greatly, resulting in premature failure of the electrode [23,24], especially when the carbon material is enshrouded by MoS_2 on a large scale [6,25]. It seems that the tactics of exposure edge sites to improve the catalytic performance of MoS_2 has reached its limitation. As a result, it is necessary and urgent to explore new and effective methods to improve the intrinsic conductivity and HER catalytic activity of MoS_2.

Owing to the characteristic of easy operation, electrochemical activation of MoS_2 has been proved to be feasible [26,27]. The mechanism of this activation strategy is mainly electrochemical removal of S atoms on the basal plane, resulting in more S vacancies with catalytic activity, in other words, it is a desulphurization process, which is similar to the creation of O vacancies in metal oxides at applied cathodic potential. Typically, for example, Tsai et al. [26] proposed that S vacancies are generated by electrochemical activation in monolayer and multilayer MoS_2 supported on different substrates. Luo et al. [28] reported an electrochemical technique in which Pd atoms were doped into the Mo sites of MoS_2, leading to the production of S vacancies on the basal plane, thus increasing the activity of the catalyst and prolonging the catalyst's life.

Herein, we successfully loaded MoS_2 nanoflowers onto GF via one-step hydrothermal method. The as-prepared composite was electrochemically activated by specific cathodic voltage. The synthesis route and electrical activation process of the composite are shown in Fig. 1a and b. The electro-activated electrode material behaves remarkable HER activity and excellent stability. The improvement of the catalytic performance can be attributed to the following three points: (i) the oxygen-containing functional groups in the GF mesh structure provide natural catalytic centers for HER; (ii) electrical activation introduces proton intercalation between MoS_2 and GF, which serves as an electronic shuttle to ensure fast electron transfer between MoS_2 and GF; and (iii) the electron density on the catalyst surface is regulated and the crystallinity of the catalyst increases, resulting in an excellent stability of the electrode.

2. Experimental section

2.1. Chemicals

Sodium molybdate ($Na_2MoO_4{\cdot}2H_2O$) and thiourea were purchased from Tianjin NO. 4 chemical reagent factory. The GF (thickness = 3 mm) and graphite rod (φ5 mm) were obtained from Beijing Jinglong special carbon graphite factory. The reagents used in the experiment belong to analytical grade and are used without further purification. Deionized water is used in the whole experiment.

2.2. Preparation of MoS_2/GF

Before preparing the composite material, GF should be pretreated. Firstly, the blank GF was immersed in acetone solution and sonicated for 30 min, washed three times by deionized water to remove the surface oil impurities, then dried in oven at 60 °C for 12 h. After that, the treated GF was placed in the muffle furnace and heated for 1 h at a temperature of 500 °C with the heating rate of 10 °C/min, the aim of this step is to create defects on the surface of GF at high temperature for facilitating the loading of catalysts. GF is used both as a substrate material for the growth of MoS_2 nanoflowers as well as a part of the composite catalysts. The nanoflowers MoS_2/GF composite was prepared by a foolproof hydrothermal method. In a typical synthesis, 1 mM $Na_2MoO_4{\cdot}2H_2O$ and 5 mM thiourea as precursors were dissolved in 60 mL deionized water, the mixture was completely dissolved by sonication for 30 min to form a uniform, colorless transparent solution, then the treated GF (3 × 3 cm^2, thickness = 3 mm) was completely immersed in the above solution for 12 h at room temperature to form a stable heterogeneous system. Then, the heterogeneous mixture was transferred to a 100 mL teflon-lined autoclave and

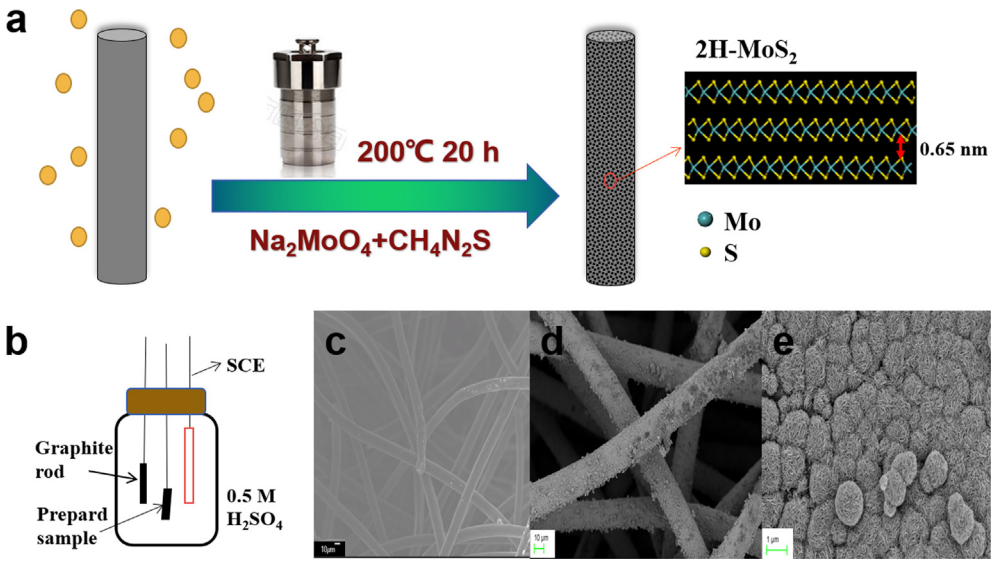

Fig. 1. (a,b) Schematic illustration of the growth of MoS_2 nanoflowers on GF and activation process. SEM images of (c) bare GF and (d,e) MoS_2/GF.

maintained at 200 °C for 20 h. After natural cooling to room temperature, the composite was clamped out and cleaned with anhydrous ethanol and deionized water for three times, respectively. Finally, the composite was dried in the oven at 60 °C for 12 h, which was labeled as MoS_2/GF. The corresponding MoS_2 powders were prepared in the same way excepting without GF.

2.3. Electrical activation process

The electrical activation process of MoS_2/GF was implemented on the electrolytic cell by a CHI760E electrochemical workstation (CH Instruments Inc., USA) at room temperature. A typical three-electrode configuration was applied with MoS_2/GF serving as working electrode, a graphite rod (φ5 mm × 20 mm) as counter electrode and a saturated calomel electrode (SCE) (φ12 mm × 120 mm, 232-01, Shanghai Leici) as the reference electrode, 0.5 M H_2SO_4 was selected as electrolyte. The activated MoS_2/GF (abbreviated as a-MoS_2/GF) was obtained by applying cathodic voltage. As a comparison, the corresponding MoS_2 and blank GF were activated in the same way. All potentials are referenced to the SCE.

2.4. Electrochemical measurements

The electrocatalytic HER and related electrochemical measurements were performed on the above three electrode system, and 0.5 M H_2SO_4 was selected as electrolyte. All potentials are referenced to the SCE. Before the measurement, the electrode was activated to a stable state by using 3000 voltammetry cycles (range from −0.3 to 0 V) with a scan rate of 100 mV s^{-1} in the same three-electrode system described above to clean the electrode to promote the balance of the electrode in the electrolyte system. The linear sweep voltammetry (LSV) curves were collected from −0.6 to 0 V with a scan rate of 5 mV s^{-1} in the case of N_2-saturation. The Nyquist plots of electrochemical impedance spectroscopy (EIS) were carried out in above cell system where the initial potential was set −200 mV (open circuit voltage, OCV, vs RHE) with frequencies varying from 100 kHz to 0.05 Hz with potential amplitude of 5 mV. The impedance data simulated by the ZView 2.0 software (Scribner Associates Inc., USA) were fitted to a simplified Randles circuit to obtain series of charge transfer resistances (R_{ct}). The Tafel plots were tested with a scan rate of 5 mV s^{-1}. The Tafel equation is $\eta = b^*\log j + a$, where η represents overpotential, j donates the current density, b is the Tafel slope, and a is the Tafel constant, the Tafel slopes can be obtained by drawing the Tafel plots. The exchange current density (j_0) can be obtained from the intercept of the linear Tafel plots to the x-axis (where the thermodynamic oxidation-reduction potential reaches 0). The formula for calculating the turn over frequency (TOF) follows: TOF = I/Q, where I denotes the current of the polarization curve measured by LSV, the voltammetric charge (Q) is calculated by the following equation: $Q = 2FN$, where F is the Faraday constant (96480 C mol^{-1}), N is the number of active sites, the value of Q is determined after deducting the blank value. The derivation and calculation of Q value can be obtained from another formula: $Q = CU = IU/v$, where v represents the scan rate (5 mV s^{-1}) in CV, in the CV curve, I and U are constantly changing, therefore the Q value can be calculated by the integral CV curve. The Mott-Schottky plots were obtained by measuring the Impedance-Potential. The system of the relationship between the impedance (Z) and the voltage of the composite electrode was established, the capacitance (C) was calculated by the formula: $C = 1/(2\pi f R_{ct})$, where f is the fixed frequency of the voltage, which was set to 1000 Hz during the measurement, R_{ct} refers to the charge transfer resistance. The electrochemical oxidation and reduction ability of the catalyst was also analyzed by CV in a potential window ranged from −1.0 to 1.0 V with a scan rate of 5 mV s^{-1} excepting that electrolyte was replaced by 0.1 M KCl containing 5 mM $Fe(CN)_6^{4-/3-}$. Chronopotentiometry was performed at current density of 10 mA cm^{-2}. Chronoamperometry was carried out at the potential of −200 mV. During the electrochemical measurements, all the tested potentials were calibrated against the reversible hydrogen electrode (RHE) according to the following equation: $E_{RHE} = E_{SCE} + 0.059 \times pH + 0.241$ in 0.5 M H_2SO_4 unless specified otherwise.

2.5. Characterization techniques

The crystallization of composite was investigated on RigakuD/Maxr-A X-ray diffractometer (XRD). The morphologies of samples were recorded via scanning electron microscope (SEM, ZEISS 1550VP) coupled with energy dispersive X-ray spectroscopy (EDS) and high-resolution transmission electron microscope (HRTEM, JEOL JEM-ARM200CF), respectively. The structures of samples were investigated by infrared spectrum (IR) on a VERTEX 70 Fourier transform infrared spectroscopy (Bruker Co., Germany) and Raman scattering spectrum on a RM-1000 Micro Raman spectroscopy (Renishaw Co., UK). Total photoluminescence (PL) spectroscopy (integrating from 600 to 800 nm) was obtained with the laser beam (488 nm) to further analyze the structure of MoS_2. The valence states of each component on the composite were studied by X-ray photoelectron spectroscopy (XPS) on an ESCALAB 250 spectrometer (Thermo, USA). The Brunauer-Emmett-Teller (BET) surface area of the materials was measured using a Surface Area and Porosity Analyzer (ASAP 2020 PLUS HD88, Micromeritics, Shanghai). The composite was cut into 5 × 5 mm^2 pieces for the SEM, XRD, XPS and Raman analysis, and ground into powder for the IR, PL, TEM and BET analysis.

2.6. Density functional theory computations

All computations were conducted within the framework of density functional theory (DFT) as fulfilled in CASTEP with the general gradient approximation (GGA) in the Perdew-Burke-Ernzerhof (PBE) type to display the exchange-correlation energy. The plane-waves cutoff energy of 320 eV and the conjugate gradient algorithm were chosen to evaluate the electronic ground state with a convergence threshold of 2.0×10^{-6} eV/atom. The tolerance for structural optimization was fixed at 2.0×10^{-5} eV/atom for energy and 0.05 eV/Å for force. For the MoS_2/GF models, the Gamma-centered 6 × 6 × 1 k-point grid was chosen for the geometry optimization, which was converged to 0.01 eV/Å. The activity of HER was reflected by the Gibbs free energy change (ΔG_{H^*}) according to the formula: $\Delta G_{H^*} = \Delta E_{H^*} + \Delta E_{ZPE} - T\Delta S$, $\Delta E_{H^*} = E_{(surface+H^*)} - E_{surface} - 1/2E_{H2}$, among of them, $E_{(surface+H^*)}$ and $E_{surface}$ are total energy of the surface model with and without H* adsorption, respectively. E_{H2} is the energy of molecular H_2 in the gas phase. Zero-point energy change ΔE_{ZPE} is obtained via vibrational frequency calculation. At 1 bar and 300 K, $T\Delta S$ is approximately −0.2 eV.

3. Results and discussion

The electrocatalytic HER at the MoS_2/GF electrode was investigated in 0.5 M H_2SO_4 solution with N_2-saturation by the three-electrode device mentioned above. Fig. 2a shows the polarization curves of the original and electrically activated MoS_2/GF (abbreviated as a-MoS_2/GF) composite measured by LSV. In this work, the activation time was determined to be 1 h by optimization. When the voltage of −0.8, −1.0 and −1.2 V was applied, the overpotential (η) of MoS_2/GF was −235, −82 and −96 mV at the current density of −10 mA cm^{-2}, respectively. Therefore, −1.0 V was determined

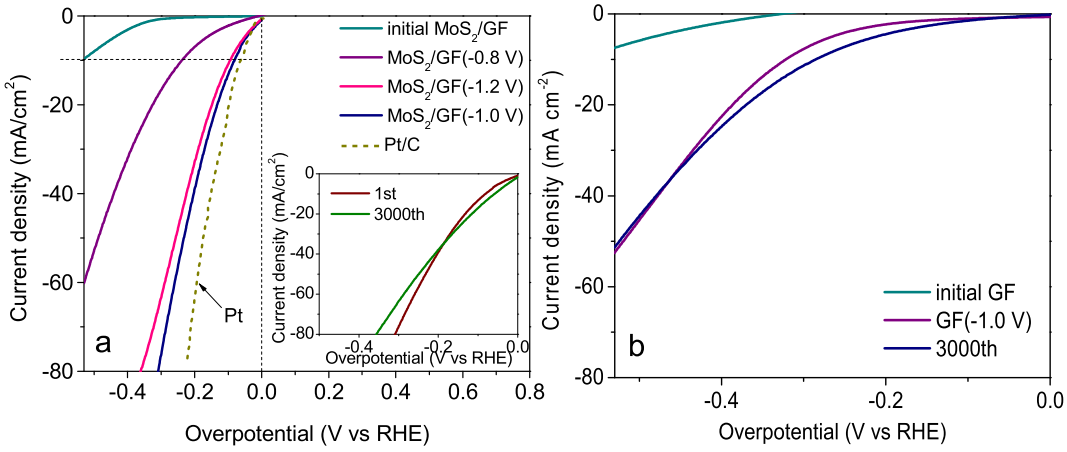

Fig. 2. Polarization curves of (a) initial MoS_2/GF, MoS_2/GF activated with different voltage and Pt/C and (b) initial GF, GF activated at optimal voltage in 0.5 M H_2SO_4 at a scan rate of 5 mV s^{-1}. Inset shows the polarization curves of MoS_2/GF activated with −1.0 V after 3000 cyclic voltammetry scans at a scan rate of 5 mV s^{-1}.

as the optimal activation voltage. Of note, the worse activation effect greater than −1.0 V may be attributed to the excessive voltage leads to the surface of the substrate GF destroyed, namely, carbon corrosion, which has been reported in the literature [29]. At −1.0 V, the a-MoS_2/GF showed lower overpotential (−308 mV) even at the current density of −80 mA cm^{-2}, which demonstrates the a-MoS_2/GF electrode exhibits better electrocatalytic HER performance compared with the original MoS_2/GF (−530 mV at the current density of −10 mA cm^{-2}). As a comparison, the HER performance of blank GF was also tested (Fig. 2b). Under the optimal activation voltage, the HER performance of blank GF was also improved, and the overpotential of −320 mV was observed at the current density of −10 mA cm^{-2}. Obviously, this value is much higher than that of the a-MoS_2/GF electrode. For comparison, the electrocatalytic HER performance (−67 mV at current density of −10 mA cm^{-2}) of commercial Pt/C (20%) electrocatalyst was also performed under the same conditions.

To compare the oxidation/reduction characteristics of GF and MoS_2/GF in the process of electrical activation, the CV experiments were performed. The intrinsic electrochemistry of blank GF is shown in Fig. S1a with increasing potential ranges from −1.0 to 1.0 V, the low and stable background capacitance is observed, no intrinsic peaks are discovered, indicating that the original GF is electrochemically inactive between −1.0 and 1.0 V where H_2 evolution occurs [30–33]. After electro-activation, a well-defined HER current appears in GF, indicating that a-GF has obvious electrocatalytic activity of HER. The initial HER overpotential of a-MoS_2/GF is close to −330 mV (Fig. S1b), which is obviously lower than that of original MoS_2/GF, and a-MoS_2/GF exhibits the maximum limited current compared with GF, a-GF and MoS_2/GF, indicating that a-MoS_2/GF has stronger catalytic activity. According to the CV curves, the corresponding TOFs were further obtained to study the number of catalytic active centers of the catalyst. It can be seen from the Fig. S1c that under the 400 mV overpotential, the TOF values of GF, a-GF, MoS_2/GF and a-MoS_2/GF are 0.14, 0.41, 0.39 and 1.11 s^{-1}, respectively, indicating that a-MoS_2/GF hold the largest number of active sites [34,35]. The CV measurements with scan rate range of 20–180 mV s^{-1} were carried out to evaluate the double-layer capacitance (C_{dl}), because the electrochemically effective surface area is directly proportional to C_{dl}. Upon fitting of the linear plots in Fig. S2d ($\Delta j = (j_a - j_b)/2$, where j_a and j_b represent current densities in CV at a certain potential: 0.15 V vs SCE), the C_{dl} values of GF, MoS_2/GF and a-MoS_2/GF are calculated as 0.605, 0.695, and 0.951 mF cm^{-2}, respectively. The increased C_{dl} values imply larger effective electrochemical surfaces of a-MoS_2/GF sample [1,34,36].

The electron transfer properties of different electrode materials were investigated by the EIS test. Fig. 3a shows AC impedance plots of the GF and MoS_2/GF in the Nyquist form. Randle equivalent circuit is employed to establish a quantitative fitting of the impedance plot. All the curves in Nyquist plot show typical semicircle patterns. At high frequency, the intercept of the real part (Z') signifies the ohmic resistance (R_s) of the electrode material and solution [37–39]. In the same reaction system, the R_s value reflects the electrical conductivity from electrode material and electrolyte [30]. For blank GF, a-GF, MoS_2/GF and a-MoS_2/GF, the fitted R_s values are 0.8203, 0.8489, 0.5773 and 0.577 Ω, respectively. Obviously, whether for GF or MoS_2/GF, the electrical conductivity from the electrode and electrolyte is almost the same after activation, which cannot provide a strong support for different HER performance. The diameter of semicircle in the Nyquist curve stands for the polarization resistance (i.e. charge transfer resistance R_{ct}) originating from the electron transfer to get over the activation barrier in the electrode reaction [40,41]. It is worth noting that the R_{ct} of H^+ between the electrode and electrolyte interface is an important parameter in the HER process in analog circuits [34,42]. The R_{ct} values of a-GF (15.52 Ω) and a-MoS_2/GF (5.047 Ω) are obviously lower than the original values, which is in accordance with the increased HER efficiency, demonstrating the best electrical integration of a-MoS_2/GF among these electrodes [34,43]. In addition, the smaller R_{ct} value would contribute possibly to modulate the electronic structure of electrode material [1]. For further affirmance, the Mott-Schottky plots (Fig. 3b) of different electrocatalysts are presented to estimate the carrier density of the samples. The fitting slopes of the four curves are all positive, indicating that these electrode materials have n-type semiconductor characteristics [34,44]. The curve slopes in the plot show that the electron concentration in a-MoS_2/GF is the highest in all samples, demonstrating that the activation process provides more surface free electrons to the material, thereby accelerating electron transport during the catalytic process [1,41].

The Tafel slopes (Fig. 3c) of different samples are given to further analyze the reaction pathway of HER, the results show that the linear slope of a-MoS_2/GF sample is 48 mV dec^{-1}, which is close to the theoretical value of 40 mV dec^{-1}, indicating that the Volmer-Heyrovsky reaction path ($H_{ads} + H^+ + e^- \rightarrow H_2$) is a rate-limiting step with the electrochemical desorption of hydrogen [45], and the similar conclusion was confirmed by Liu et al [1]. Fig. 3d summarizes the recent reported HER kinetic data of many MoS_2-based electrocatalysts in acidic media [6,8,46–55], in which the a-MoS_2/GF sample exhibits the considerable electrocatalytic HER performance, especially in the low Tafel slope of 48 mV dec^{-1}.

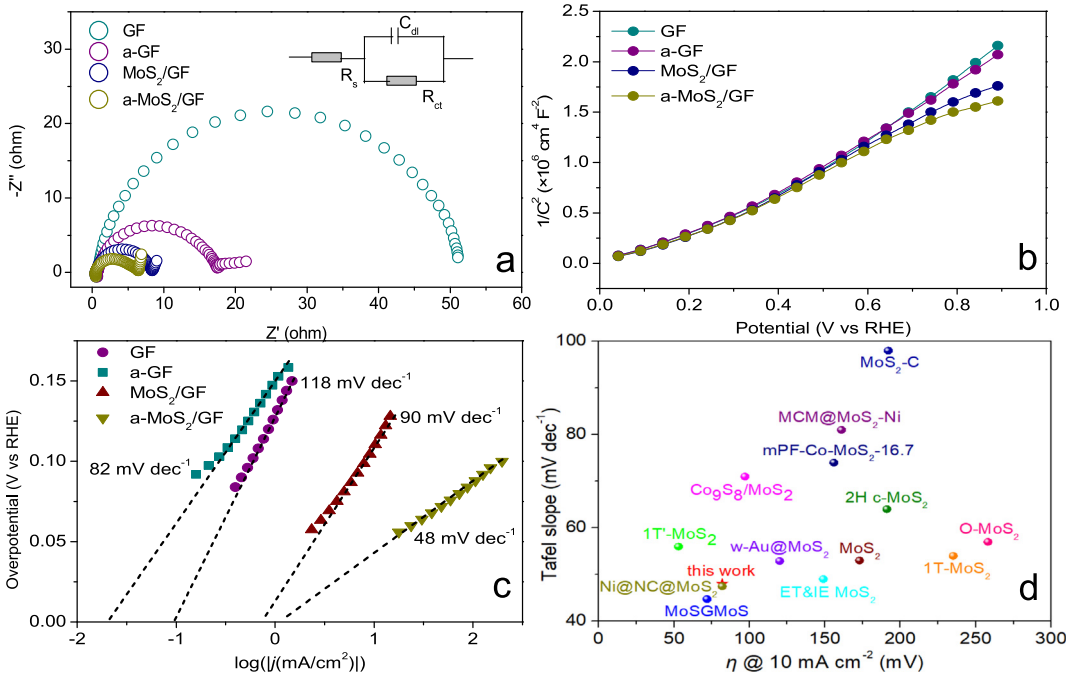

Fig. 3. (a) Nyquist plots; (b) Mott-Schottky plots; (c) Tafel plots of the GF, a-GF, MoS_2/GF and a-MoS_2/GF; and (d) Comparison of the overpotentials at −10 mA cm^{-2} and the Tafel slopes of recently reported MoS_2-based electrocatalysts [6,8,46–55].

The lower Tafel slope illustrates that the HER rate of a-MoS_2/GF electrode will increase rapidly with the increase of overpotential, which will have a great competitive advantage in practical HER applications [45,56]. The Tafel slope is less dependent on the density of the catalytic active sites, and the Tafel slope is usually between 65–75 and 65–85 mV dec^{-1} for the edge sites and S vacancies in the MoS_2, respectively. The Tafel slope may become larger when the active site density decreases [57]. Therefore, it can be concluded that one of the main reasons for the enhancement of MoS_2/GF catalytic activity after activation is the increase of the active site density. Exchange current density (j_0) is also an important parameter for characterizing the intrinsic properties of synthetic composite, which can be obtained from the Tafel plots. As shown in Table S1, the exchange current density of a-MoS_2/GF is 1222 μA cm^{-2}, which is superior to all the tested samples, suggesting that a-MoS_2/GF requires a lower driving force to initiate the reaction, which further confirms the strongest HER kinetics at the a-MoS_2/GF electrocatalyst interface. The high exchange current density can be attributed to the disorder degree and uneven morphology of activated MoS_2 on GF, which can provide more effective active sites to facilitate the reaction [58,59].

Undergoing 3000 times voltammetry cycles, the polarization curves of both a-MoS_2/GF and a-GF move slightly to the positive direction at the current density of −10 mA cm^{-2} (inside Fig. 2a and b). On the one hand, it shows that the CV cycles have a slight activation effect on the electrode, which is also in line with the previous literature [60]. On the other hand, the electrode material has good electrochemical stability in acid solution.

Long-term stability is also a vital factor in evaluating the stability of electrode material. In this work, the stability of electrode material was measured by chronopotentiometry and chronoamperometry methods. The stability of the catalyst was determined by chronopotentiometry via evaluating the ability to maintain the cathodic current for 10 mA cm^{-2} within 12 h (Fig. S3a), where a-MoS_2/GF shows lower potential and maintains good stability. The original MoS_2/GF catalyst shows the initial decay before running for 8 h (−178 mV@8h vs. 127 mV@0h) for HER performance, beyond 8 h, the potential of MoS_2/GF maintains stability with time up to 12 h. Herein, original MoS_2/GF exhibits lower overpotential than a-MoS_2/GF in the initial period, which may be due to improved interfacial contact and MoS_2 leaching that may occur on the surface of MoS_2/GF. Meanwhile, the H_2 bubble movement accelerates the slight oxidation of the original MoS_2 sites, resulting in a lower initial overpotential [61]. It's worth noting that the potential of MoS_2/GF is close to a-MoS_2/GF and finally reaches the same saturation value, which can be attributed to that at the applied activation voltage, with the electrochemical activation of the high binding energy S_2^{2-} sites, the MoS_2 layer becomes roughened during the irreversible reaction [61]. On the other hand, it indicates that MoS_2/GF is also activated under the action of electricity, which is consistent with the above results. However, the potential of a-GF has almost no change compared with the initial GF. The chronoamperometry was carried out separately under the potential of −200 mV, the test results are shown in Fig. S3b, and a-MoS_2/GF shows the highest current density (about −49 mA cm^{-2}).

For exploring the mechanism of HER performance enhancement induced by electro-activation on MoS_2/GF electrode, now it focuses on the structure analysis of the electrode materials. The Fig. 4a shows the XRD plot of the original MoS_2/GF and a-MoS_2/GF samples. Three diffraction peaks are observed at 14°, 33°, 42.78°, corresponding to the (0 0 2), (1 0 0) and (1 0 3) planes of 2H-MoS_2 (PDF 73-1508), respectively, which is consistent with previous literatures [62,63]. The broad peak at 2θ = 25.0° is the typical diffraction peak of carbon material (PDF 75-1621) [30]. It is to be noted that an obvious enhancement of diffraction peak at 2θ = 58.4° on a-MoS_2/GF, which corresponds to the (1 1 0) plane of MoS_2 (PDF 73-1508) [62,63]. To the best of our knowledge, at 2θ = 14°, the existence of the (0 0 2) peak represents the stacking slabs along the *c*-axis, while the presence of the (1 1 0) peak at 2θ ≈ 59° is representative of a slab layer [64]. For the original MoS_2, the diffraction peak at (0 0 2) is very sharp and strong due to good crystallinity and volume properties [45]. Here, the diffraction peak of (0 0 2) has no obvious change before and after activation,

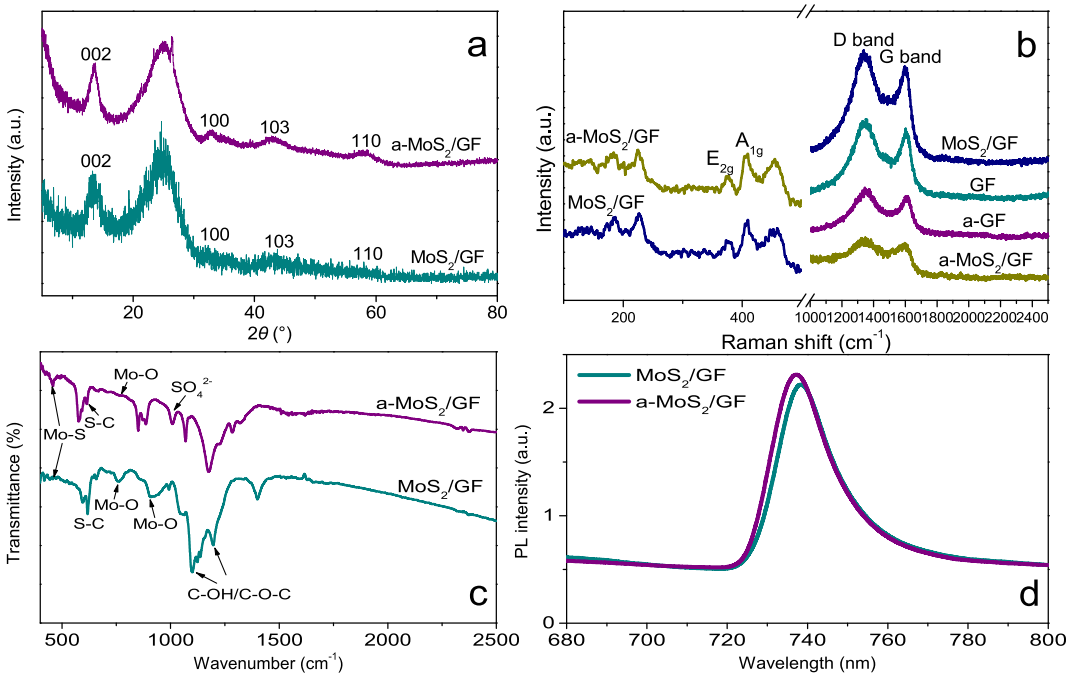

Fig. 4. (a) XRD patterns; (b) Raman scattering spectra; (c) FT-IR spectra; and (d) PL spectra of MoS_2/GF and a-MoS_2/GF.

indicating that the crystal structure of MoS_2 does not be destroyed during activation, while the enhancement of diffraction peak of (1 0 0) shows that the compactness between MoS_2 increases after electro-activation.

The existence of carbon support was confirmed by Raman spectroscopy (Fig. 4b) and the characteristic peaks of Mo compounds were detected. It is noted that there are significant differences in Raman spectra between GF and MoS_2/GF after electro-activation. The Raman intensities of a-GF and a-MoS_2/GF are both lower than the initial value, the change of Raman intensity in MoS_2/GF is blatant than that of GF, suggesting that the multi-reflection and interference of the incident and scattered light induced by the substrate are suppressed on the thick and opaque GF [65,66]. All the samples show strong absorption peaks at 1342 and 1604 cm^{-1}, which corresponds to the typical D and G bands on GF [30]. The D band is derived from the structural defects of carbon material related to vacancy, grain boundary and amorphous carbon species, the G band is considered to the E_{2g} model of sp^2 carbon [55,67]. After electro-activation, the ratio of I_D/I_G in GF increases from 1.11 to 1.19, indicating the increase of sp^3 defects in sp^2 carbon network due to the functionalization of carbon atoms [30], while the ratio of I_D/I_G in MoS_2/GF changes slightly (from 1.14 to 1.13), suggesting the enhancement of catalytic activity in MoS_2/GF is not dominated by the surface defects of GF, which also corresponds to the invariance of the (0 0 2) base peak in XRD. In the Raman spectra, the two main Raman peaks at 376.3 and 408.2 cm^{-1} correspond to the E^1_{2g} and A_{1g} modes in 2H-MoS_2, respectively [68]. The former peak (E^1_{2g}) originates from the in-plane vibrations and the latter one (A_{1g}) from the vertical-plane vibrations of the Mo-S bond in MoS_2, the separation between these two peaks is mainly dependent on the layer number in MoS_2 nanosheets [61]. Obviously, no detectable shift on E^1_{2g} and A_{1g} modes is observed after electro-activation, which means that MoS_2 grown on GF is the optimally doped, no further doping is introduced into MoS_2 by activation [69]. In other words, the activated electrode material still maintains a high quality of crystallization. Besides, it also rules out the possibility of phase transition from 2H-MoS_2 to 1T-MoS_2, which can greatly improve the catalytic performance and introduce obvious changes in Raman spectra [60]. Therefore, it can be inferred that the improvement of catalytic activity of MoS_2/GF after electrical activation does not originate from the generation of new active sites, but from the catalytic activity enhancement of existing active sites, which can be further confirmed by the later Gibbs free energy. The FT-IR spectra of MoS_2/GF before and after activation were recorded (Fig. 4c). The peak at ~458 cm^{-1} corresponds Mo—S band, and the Mo—O peak (~765 cm^{-1}), S—C peak (~615 cm^{-1}) could be observed [70,71]. After activation, the intensity of Mo-S band increases. The intensity of Mo—O peak and S—C peak decrease, and the intensities of C—OH/C—O—C peaks (1097 and 1195 cm^{-1}, generally two peaks) [70] are also obviously weakened. It can be inferred that during activation, the interaction between these functional groups has a positive impact on HER performance.

In order to determine the uniformity of the MoS_2 on the GF, PL spectrum (integrated over the 680–800 nm region) was carried out. As shown in Fig. 4d, it is almost uniform, indicating that MoS_2 grows homogeneously on GF surface, and Paul et al. also demonstrated this opinion [69], which can also be demonstrated by the following SEM images. There is a significant intensity enhancement and a slight blueshift in the MoS_2/GF after activation. The enhancement of PL intensity in a-MoS_2/GF is quite interesting. Generally, MoS_2 and carbon material form type-II heterojunction with convenient charge transfer, which usually leads to PL quenching, therefore it is considered to be an effective choice for photocatalyst [69,72]. During the in-situ hydrothermal growth of MoS_2 on GF, the S atom can replace the O atom in the reticular structure of GF, resulting in the S-doped GF, which leads to the enhancement of electron density on the surface of GF. And the corresponding PL intensity increases [69], which is also demonstrated by the following fitted O 1s spectrum of XPS in MoS_2/GF, where the area percentages of C═O/O—C═O and C—OH/C—O—C reduce. On the basis of previous reported literature, the enhancement of PL intensity and blueshift can be also derived from the p-doping in the MoS_2 layers [60], which has been proved that most of the trions (excess electron bound on the neutral exciton) in p-doped MoS_2 are transferred via the interface between MoS_2 and substrate [69]. Therefore, the charge transfer via MoS_2 and GF interface is more

similar to the typical p-doping process of chemical and physical treatment owing to the interfacial migration of loosely bound electrons (excess electrons), and the p-doping effect of the MoS_2 shell leads to the enhanced PL intensity [69]. This p-doping is also supported by XPS measurements, the survey spectrum of XPS clearly indicates the existence of S, Mo, C and O (Fig. S4a), p-doping results in shifts of 0.5 and 0.3 eV in the Mo 3d and S 2p peaks (Fig. S4b). The shift of binding energy is consistent with that of p-doped MoS_2 reported in the past [60]. Howbeit, the Raman spectra have confirmed that the prepared MoS_2 belongs to the optimal doping, no new doping is introduced after electrical activation, so the doping is inferred to be between MoS_2 and substrate GF.

To further investigate the surface chemistry of the electrode material, XPS fitting analysis is presented. As shown in Fig. S5a, two major peaks are observed at ~ 229.0 and 232.6 eV, which correspond to Mo $3d_{5/2}$ and Mo $3d_{3/2}$ in Mo (IV), respectively, indicating that MoS_2 is dominant in the prepared sample. A relatively weak peak at 234.2 eV is also observed from Mo (VI), demonstrating a slight oxidation on the MoS_2 surface [45,55]. The peaks at ~ 228.4 and ~ 231.3 eV are defined as Mo—C bond [73], and the Mo-O peak locates at 230.6 eV [74], which is formed by the coordination of Mo atoms with carboxylic acids and/or carbonyl groups according to the decreased area percentages of C—OH/C—O—C and C═O/O—C═O in the C 1s and O 1s spectra of GF and MoS_2/GF (Figs. S6 and S7) [30]. The presence of Mo—O and Mo—C bonds allows MoS_2 to participate in electron transfer on the surface of GF. However, the area percentages of these two bonds decreases (Table S2) after electrical activation, so the enhancement of catalytic activity has little relation with Mo-related groups. Therefore, it must consider the influence of S site. In Fig. S5b, two main characteristic peaks are observed at 162.2 and 163.4 eV, which correspond to S $2p_{3/2}$ and S $2p_{1/2}$, respectively [1]. After electrical activation, the binding energies of some parts of S 2p show a slight negative shift, demonstrating the increase of electron density in MoS_2 after activation [75]. Two new shoulder band peaks appear in activated MoS_2. The whole electron spectroscopy is refitted to 161.9/163.1 eV and 163.4/164.6 eV, lower binding energy doublets are assigned to unsaturated S^{2-} and terminal S_2^{2-}, the higher binding energy doublets can be assigned to bridging S_2^{2-} and apical S^{2-} [69]. It is noteworthy that the bridging S_2^{2-}/apical S^{2-} increases from 1.04 to 1.82 after electrical activation, and this increase has been confirmed to promote the HER process [61]. The existence of S^{2-} in a-MoS_2/GF sample may correspond to the S—C bond formed when O atoms in GF meshes are replaced by S atoms, leading to S-doped GF [69], which is also demonstrated by the S—C peak in the fitted S 2p and C 1 s spectrum in MoS_2/GF. This is consistent with what PL observed. After activation, the relatively content of S—C bond decreases (Figs. S5b and S6b, Tables S2 and S3), while the S—O bond increases obviously (Figs. S5b and S7b, Tables S2 and S3), indicating that the electron transfer pathway is mainly through the S site in MoS_2 and the oxygen-containing functional groups on the GF surface, allowing MoS_2 to participate in the electron transfer of GF catalytic centers.

The SEM images (Fig. 5a and b) reveal the flower-like structure of the as-prepared sample, which is consistent with the results of the preparation method used for reference in this work [17]. The flower-like MoS_2 can be successfully grown on GF, mainly originating from the large number of porous centers in the GF, which not only act as the nucleation sites of the MoS_2, but also facilitate the aggregation of the MoS_2 in GF, thereby growing the better flower-like structure [61]. The MoS_2 sample remain intact flower-like structure after electrical activation (Fig. 5c and d), consisting of many 2D nanosheets, while the distance between the

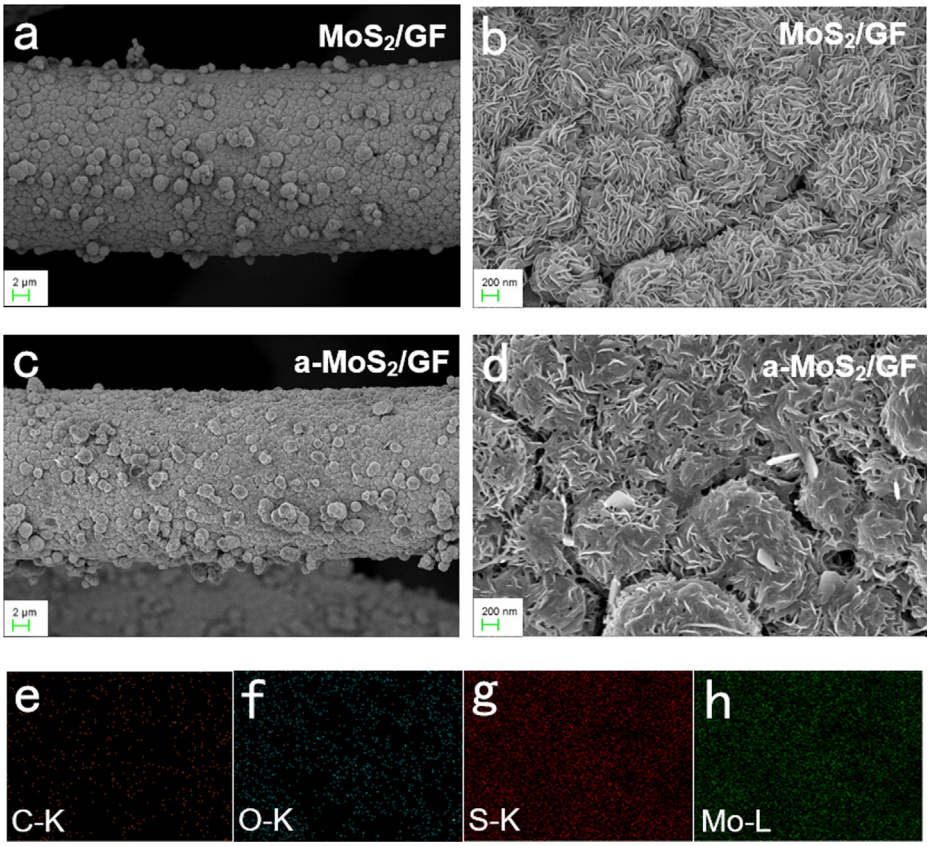

Fig. 5. SEM images of (a,b) MoS_2/GF and (c,d) a-MoS_2/GF. (e-f) Corresponding EDS mappings of C, O, S and Mo elements of MoS_2/GF.

adjacent flower-like structures becomes more compact. The corresponding EDS mapping analysis (Fig. 5e–h) clearly reveals the Mo, S, C, O in the composite distribute homogeneously over the selected regions. EDS spectra demonstrates that the stoichiometric ratio of S:Mo increased from 1.57 to 2.23 after electrical activation (Fig. S8), which is also consistent with the results of Fig. S4b. Thus, it is suspected that the electrochemical activation process could lead to the formation of Mo site defects. This increase in the S site has been clarified to be conducive to charge transfer in the material [76]. As shown in the TEM images (Fig. 6a and b), distinct petal structure can be observed, and Fig. 6b shows obvious corrugations and ripples, demonstrating the ultrathin characteristic of MoS_2 nanoflowers [58]. The lattice fringes with 0.65 nm in cross-sectional TEM images correspond to the (0 0 2) basal plane in the 2H-MoS_2 [74], which is consistent with the XRD patterns. Moreover, the thickness of nano-petal is determined as 5–10 nm, corresponding to 5–10 sandwiched S-Mo-S layers. Accompanied by the electrical activation, the fringes of the curled edges become more continued and the spacing of lattice fringes increases (Fig. 6e). On the one hand, the higher crystallinity is suggested; on the other hand, electrical activation leads to the expansion of MoS_2 layer spacing, and modulates the surface electronic state of MoS_2 to enhance its intrinsic electrical conductivity, which is beneficial to the faster electron transfer between the active sites in GF [45,58]. Fig. 6c and f display the selected area electron diffraction (SAED) images of MoS_2/GF and a-MoS_2/GF, the subtle changes in the degree of disorder before and after activation can still be judged. For MoS_2/GF, the atomic arranging manners on the basal plane are strongly disordered, in which even short-range ordering of nanodomains could not be clearly observed (Fig. 6c). After electrical activation, small nanodomains with short-range ordering emerges in the manner of aperiodic arrangement (Fig. 6f). The unique arrangement of nanodomains can partially retain the 2D electron conjugation along the basal plane, resulting in fast interdomain electron transport [58].

The N_2 adsorption-desorption measurements were performed to investigate the textual properties of the samples. The type Ⅱ characteristic adsorption isotherm is observed in bare GF with a highest BET surface area of 110.478 $m^2\ g^{-1}$ with the corresponding total pore volume 0.059 $cm^3\ g^{-1}$ at P/P_0 = 0.995 (Fig. S9a), and a bimodal curve whose peaks are centered at ca. 11.2 and 15.3 nm is observed in the pore size distribution of GF (inside Fig. S9b), revealing the mesopore nature of GF, while MoS_2/GF and a-MoS_2/GF approximate the type IV feature with noticeable type H3 hysteresis loop. The BET surface areas of MoS_2/GF and a-MoS_2/GF are determined to be 68.49 and 3.70 $m^2\ g^{-1}$ with their total pore volumes of 0.043 and 0.0079 $cm^3\ g^{-1}$ at P/P_0 = 0.995, respectively. Considerable diminishment in the BET surface area and total pore volume of MoS_2/GF compared with GF signifies successful functionalization with the occupation of MoS_2 nanosheets on the surface of GF fiber structure and mass increment with high density after the hydrothermal process, thereby hindering the N_2 uptake throughout the nano-porous channel. However, conversely, a-MoS_2/GF exhibits the largest average pore diameter (10.0134 nm) compared to GF (2.7086 nm) and MoS_2/GF (3.8305 nm), and the pore diameter of a-MoS_2/GF is concentrated in the range of more than 50 nm, indicating that electrical activation processes can lead to the formation of larger pores that facilitate mass diffusion/transfer during catalytic reactions [77].

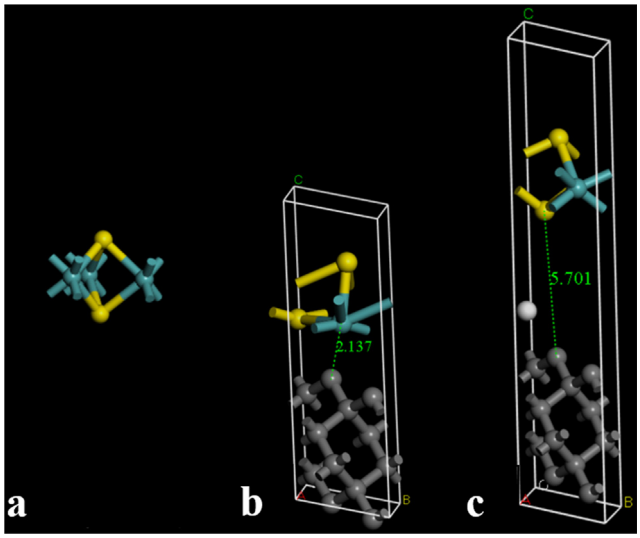

Fig. 7. Optimized geometric structures of (a) MoS_2, (b) MoS_2/GF and (c) a-MoS_2/GF. Dark cyan, yellow, gray and white spheres represent Mo, S, C and H, respectively.

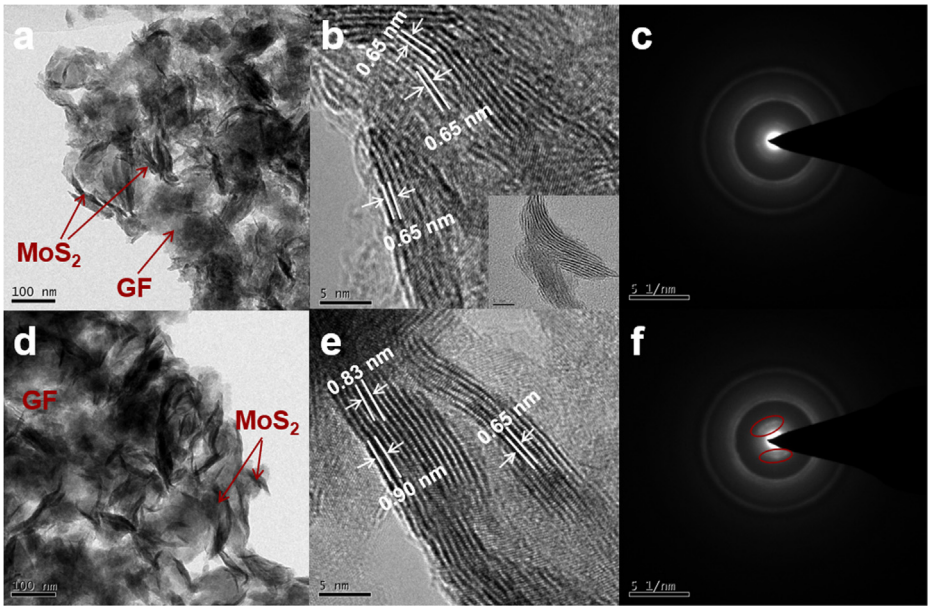

Fig. 6. HR-TEM images and SAED of (a-c) MoS_2/GF and (d-f) a-MoS_2/GF.

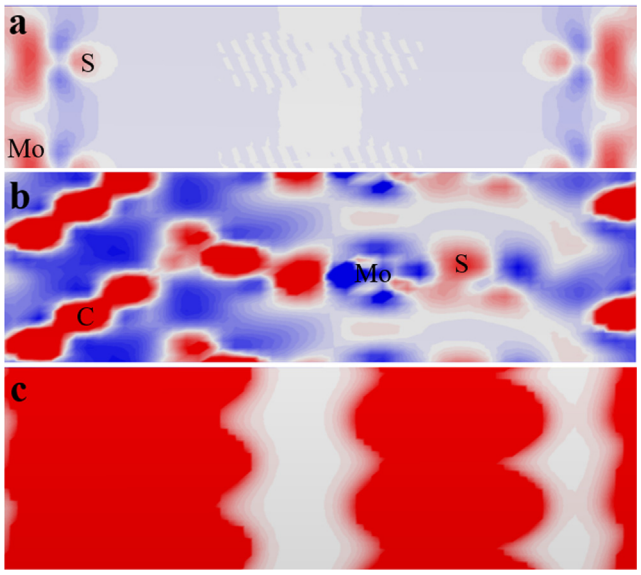

Fig. 8. The charge density distributions of (a) MoS_2, (b) MoS_2/GF and (c) a-MoS_2/GF calculated through the DFT. Blue-white-red indicates that the charge density is increased sequentially.

As discussed above, the catalytic performance of MoS_2/GF electrode is greatly improved in the process of electrical activation, the synergistic effect of the increased interlayer spacing of MoS_2 nanosheets and conductive GF is a key cause of excellent HER activity [54], and two main factors are considered: i) the electron transfer between MoS_2 and GF is enhanced; and ii) p-doping is introduced into the system during the activation process. The former has been inferred mainly due to the enhanced electron transfer between the S site in MoS_2 and the oxygen-containing functional groups on the GF surface. For further certification, MoS_2 powders were prepared under the same conditions, then Nafion, isopropanol and deionized water (62%:31%:7% by volume) were added to form a paste mixture and coated on the indium-tin-oxide (ITO) coated slide and blank GF, dried at room temperature to obtain MoS_2-bound ITO and MoS_2-bound GF electrodes. The results of LSV test are shown in Fig. S10, no significant improvement is found for activated MoS_2-bound ITO activated MoS_2-bound GF. For the latter, it can associate p-doping and improved catalytic activity of MoS_2 with protons. More specifically, it is related to protons inserted between MoS_2 and underlying GF [60]. The electrical activation of MoS_2/GF was carried out in 0.5 M Na_2SO_4 solution, where the catalytic activity of the catalyst almost unchanged (Fig. S11), which shows that the protons in acidic electrolyte form p-doping between MoS_2 and GF under the action of electricity, i.e. proton intercalation is formed, and this intercalation plays a leading role in the enhancement of catalytic activity.

DFT calculations were conducted for better comprehending the enhanced HER activity of a-MoS_2/GF. The structure of all samples was optimized in CASTEP (Fig. 7), and the lattice types and related parameters of the optimized samples are shown in Table S4. As

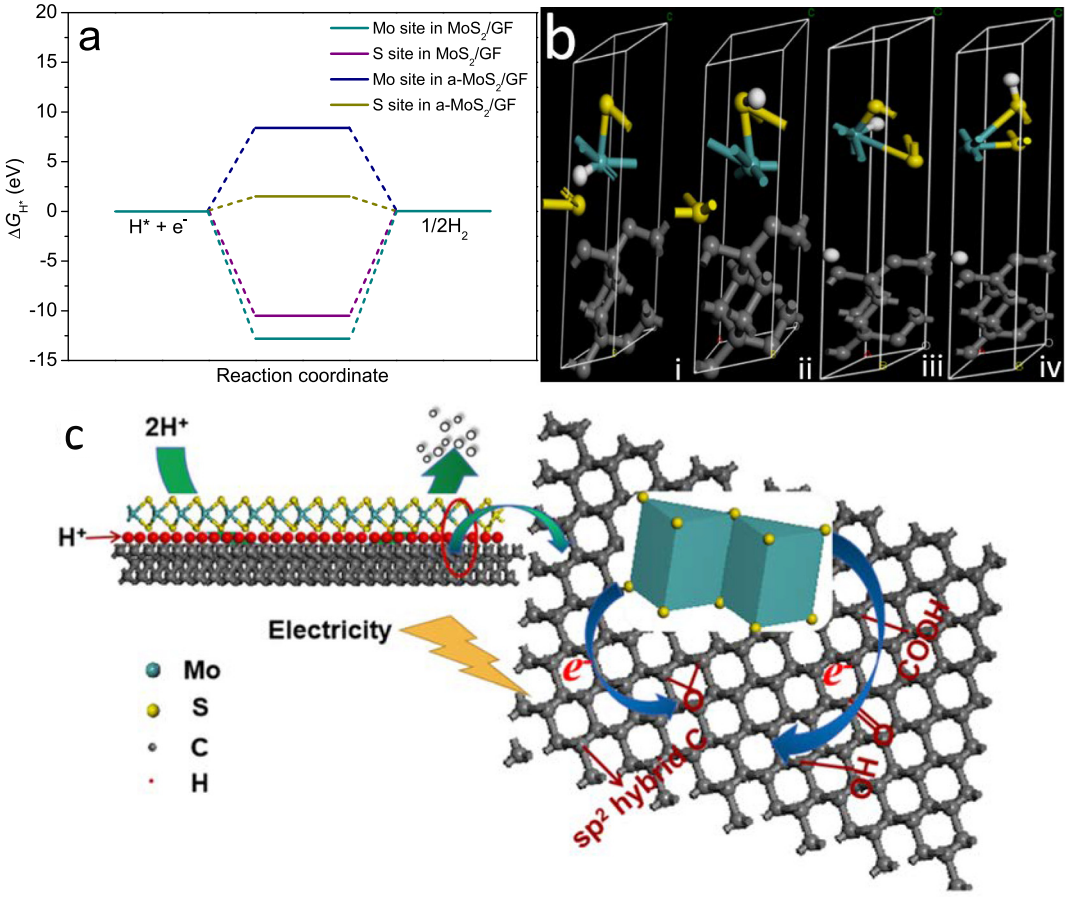

Fig. 9. (a) HER Gibbs free-energy diagram for Mo and S sites in MoS_2/GF and a-MoS_2/GF. (b) Corresponding H adsorption forms, where (i and iii) H atom adsorbed at Mo site in MoS_2/GF and a-MoS_2/GF, (ii and iv) H atom adsorbed at S site in MoS_2/GF and a-MoS_2/GF. Dark cyan, yellow, gray and white spheres represent Mo, S, C and H, respectively. (c) Proposed proton intercalation and electron transfer route at the MoS_2/GF composite cathode during electrochemical activation process.

displayed in the calculated band structure in Fig. S12, the pristine 2H-MoS_2 slab owns a bandgap of 1.67 eV, which is close to the value (1.75 eV) reported in the literature [58]. In terms of the band structure, a-MoS_2/GF exhibits a more curved band near the Fermi level, indicating that the electrons are less localized in the sample, which leads to the higher electron mobility and carrier density. This change in bandgap can be attributed to the enhanced hybridization between the Mo d-orbital and the S p-orbital after electro-activation [78]. It can be seen from the calculated density of states (DOS) that both the MoS_2/GF and a-MoS_2/GF exhibit the electronic state of the Fermi level (Fig. S13a). At the same energy level, the peak of the electronic state exhibited by a-MoS_2/GF is significantly higher than that of MoS_2/GF, indicating that a-MoS_2/GF possesses more electrons, which will generate more charge carriers, thereby improving the catalytic performance [1]. The above conclusions can also be confirmed by the partial density of states (PDOS) of Mo and S (Fig. S13b,c). Both Mo and S in a-MoS_2/GF show a distinct electronic state near the Fermi level, and the peak of electronic state of a-MoS_2/GF is higher than that of MoS_2/GF. In order to more intuitively observe the effect of electrical activation on the electronic structure of the composite, the charge density distribution was investigated. Fig. 8 clearly manifests that electrical activation contributes a great deal to charge density, which is distinct from the original charge density of MoS_2 and MoS_2/GF.

It is generally believed that the HER process includes an initial H state, an intermediate H* state, and a final $1/2H_2$ state. In order to reduce the reaction barrier between the adsorption-desorption steps, a good HER catalyst is expected to have a H adsorption free energy ΔG_{H^*} close to zero [1]. Herein, we focused on the adsorption free energy of H atom at Mo and S sites. The results are summarized in Table S5 and Fig. 9a,b, it is obvious that the ΔG_{H^*} of the H atom at the S site in a-MoS_2/GF is the smallest, indicating that H is most easily adsorbed at the S site, which is also consistent with the Raman's conclusion that the increase in catalytic activity of a-MoS_2/GF is not due to the production of new active sites, but to the enhanced catalytic activity from existing active sites. Moreover, it also demonstrated the catalytic reaction takes place preferentially at the S site. Thus, the catalytic sites in MoS_2 were effectively activated under optimized voltage.

As a result, the high HER activity as well as excellent stability of the optimized MoS_2/GF with synergistically structural and electronic modulations can be attributed to five aspects as follows: i) the active functional groups (C—OH/C—O—C and C=O/O—C=O) in the GF structure provide natural catalytic centers for HER; ii) the electron transfer between MoS_2 and GF is ensured by the Mo—C, Mo—O, S—C and S—O at the interface, and the integral 2D electron conjugation leads to fast interdomain electron transport; iii) the enhanced intrinsic conductivity of nanodomains facilitates the combination between positive protons and catalyst; iv) the relatively higher crystallinity of MoS_2 ensures the long-term stability during the electrocatalysis; and v) the protons between MoS_2 and GF act as excellent electron shuttle, resulting in a sharp increase in electron density on the catalyst surface and the rapid transport of electrons between MoS_2 and GF, and the combined modulations of active sites may open a new door for strengthening the activity of analogous electrocatalysts. Based on above analysis, the mechanism of enhanced HER performance via electrical activation process in MoS_2/GF is clarified in Fig. 9c.

4. Conclusions

In summary, a simple and rational strategy has been demonstrated to achieve an incredible enhancement of the electrocatalytic HER performance of MoS_2/GF via electrical activation at a specific voltage. The electro-activation process increases the electron density on the surface of the catalyst, and protons inserted between MoS_2 and GF act as electron shuttle, thus ensuring fast electron transfer between MoS_2 and GF via oxygen-containing functional groups, resulting in high-efficiency and stable HER performance. This straightforward method leads to favorable kinetics and proliferation of active sites in the MoS_2/GF nanostructure, which endow it with superior yet stable catalytic activity, resulting in MoS_2/GF an earth-abundant highly competitive catalyst for HER and other potential reactions. Furthermore, this general strategy through controlling nanostructures and morphology can be conducive to modifying many 2D layered composites to improve their applications in high-performance heterogeneous catalysis.

Declaration of Competing Interest

The authors declared that there is no conflict of interest.

Acknowledgements

This study was financially supported by the Program for the National Natural Science Foundation of China (51879101, 51579098, 51779090, 51709101, 51521006, 51809090, 51278176, 51378190), the National Program for Support of Top-Notch Young Professionals of China (2014), the Program for Changjiang Scholars and Innovative Research Team in University (IRT-13R17), Hunan Provincial Science and Technology Plan Project (2018SK20410, 2017SK2243, 2016RS3026), the Natural Science Foundation of Hunan Province, China (Grant Nos. 2019JJ50077) and the Fundamental Research Funds for the Central Universities (531119200086, 531118010114, 531107050978).

Appendix A. Supplementary material

Supplementary data to this article can be found online at https://doi.org/10.1016/j.jcat.2019.11.003.

References

[1] P. Liu, J. Zhu, J. Zhang, P. Xi, K. Tao, D. Gao, D. Xue, ACS Energy Lett. 2 (2017) 745.
[2] D. Huang, C. Hu, G. Zeng, M. Cheng, P. Xu, X. Gong, R. Wang, W. Xue, Sci. Total Environ. 574 (2017) 1599.
[3] D. Huang, W. Xue, G. Zeng, J. Wan, G. Chen, C. Huang, C. Zhang, M. Cheng, P. Xu, Water Res. 106 (2016) 15.
[4] W. Xue, D. Huang, G. Zeng, J. Wan, C. Zhang, R. Xu, M. Cheng, R. Deng, J. Hazard. Mater. 341 (2018) 381.
[5] L. Lei, D. Huang, G. Zeng, M. Cheng, D. Jiang, C. Zhou, S. Chen, W. Wang, Coordin. Chem. Rev. 399 (2019) 213020.
[6] Y. Li, M.B. Majewski, S.M. Islam, S. Hao, A.A. Murthy, J.G. Distefano, E.D. Hanson, Y. Xu, C. Wolverton, M.G. Kanatzidis, Nano Lett. 18 (2018) 7104.
[7] X. Gong, D. Huang, Y. Liu, G. Zeng, R. Wang, J. Wei, C. Huang, P. Xu, J. Wan, C. Zhang, Bioresour. Technol. 253 (2018) 64.
[8] S.A. Shah, X. Shen, M. Xie, G. Zhu, Z. Ji, H. Zhou, K. Xu, X. Yue, A. Yuan, J. Zhu, Y. Chen, Small 15 (2019) 1804545.
[9] D. Huang, R. Deng, J. Wan, G. Zeng, W. Xue, X. Wen, C. Zhou, L. Hu, X. Liu, X. Guo, X. Ren, J. Hazard. Mater. 348 (2018) 109.
[10] B. Guo, K. Yu, H. Li, H. Song, Y. Zhang, X. Lei, H. Fu, Y. Tan, Z. Zhu, ACS Appl. Mater. Interfaces 8 (2016) 5517.
[11] Y. Guo, X. Zhang, X. Zhang, T. You, J. Mater. Chem. A 3 (2015) 15927.
[12] Y. Yin, J. Han, Y. Zhang, X. Zhang, P. Xu, Q. Yuan, L. Samad, X. Wang, Y. Wang, Z. Zhang, J. Am. Chem. Soc. 138 (2016) 7965.
[13] J. Kibsgaard, Z. Chen, B.N. Reinecke, T.F. Jaramillo, Nat. Mater. 11 (2012) 963.
[14] D. Kong, H. Wang, J.J. Cha, M. Pasta, K.J. Koski, J. Yao, Y. Cui, Nano Lett. 13 (2013) 1341.
[15] S. Shin, Z. Jin, D.H. Kwon, R. Bose, Y.S. Min, Langmuir 31 (2015) 1196.
[16] C.B. Ma, X. Qi, B. Chen, S. Bao, Z. Yin, X.J. Wu, Z. Luo, J. Wei, H.L. Zhang, H. Zhang, Nanoscale 6 (2014) 5624.
[17] H. Wang, C. Peng, F. Wen, Z. Ying, Y. Zhang, Actuat. B-Chem. 220 (2015) 749.
[18] X. Gong, D. Huang, Y. Liu, Z. Peng, G. Zeng, P. Xu, M. Cheng, R. Wang, J. Wan, Crit. Rev. Biotechnol. 38 (2018) 455.
[19] C. Hu, D. Huang, G. Zeng, M. Cheng, X. Gong, R. Wang, W. Xue, Z. Hu, Y. Liu, Chem. Eng. J. 338 (2018) 432.
[20] H. Wang, Z. Lu, S. Xu, D. Kong, J.J. Cha, G. Zheng, P.C. Hsu, K. Yan, D. Bradshaw, F.B. Prinz, Proc. Natl. Acad. Sci. USA. 110 (2013) 19701.

[21] G.R. Bhimanapati, T. Hankins, Y. Lei, R.A. Vilă, I. Fuller, M. Terrones, J.A. Robinson, ACS Appl. Mater. Interfaces 8 (2016) 22190.
[22] Y. Li, H. Wang, L. Xie, Y. Liang, G. Hong, H. Dai, J. Am. Chem. Soc. 133 (2011) 7296.
[23] C. Chen, X. Xie, B. Anasori, A. Sarycheva, T. Makaryan, M. Zhao, P. Urbankowski, L. Miao, J. Jiang, Y. Gogotsi, Angew. Chem. Int. Ed. 57 (2018) 1846.
[24] X. Liu, D. Huang, C. Lai, G. Zeng, L. Qin, H. Wang, H. Yi, B. Li, S. Liu, M. Zhang, R. Deng, Y. Fu, L. Li, W. Xue, S. Chen, Chem. Soc. Rev. 48 (2019) 5266.
[25] C. Zhang, W. Wang, A. Duan, G. Zeng, D. Huang, C. Lai, X. Tan, M. Cheng, R. Wang, C. Zhou, W. Xiong, Y. Yang, Chemosphere 222 (2019) 184.
[26] C. Tsai, H. Li, S. Park, J. Park, H.S. Han, J.K. Nørskov, X. Zheng, Nat. Commun. 8 (2017) 15113.
[27] X. Guo, Z. Peng, D. Huang, P. Xu, G. Zeng, S. Zhou, X. Gong, M. Cheng, R. Deng, H. Yi, H. Luo, X. Yan, T. Li, Chem. Eng. J. 347 (2018) 74.
[28] Z. Luo, Y. Ouyang, H. Zhang, M. Xiao, J. Ge, Z. Jiang, J. Wang, D. Tang, X. Cao, C. Liu, Nat. Commun. 9 (2018).
[29] M. Qiao, Y. Zhang, L. Zhai, M. Sun, Chem. Eng. J. 344 (2018) 410.
[30] L. Lei, L. Fang, L. Zhai, R. Wang, M. Sun, Electrochim. Acta 261 (2018) 394.
[31] S. Chen, D. Huang, G. Zeng, X. Gong, W. Xue, J. Li, Y. Yang, C. Zhou, Z. Li, X. Yan, T. Li, Q. Zhang, Chem. Eng. J. 370 (2019) 1087.
[32] T.S. Min, A. Adriano, S. Zden, K.H. Těpán, S. David, P. Martin, Chemistry 21 (2015) 7170.
[33] D. Huang, X. Guo, Z. Peng, G. Zeng, P. Xu, X. Gong, R. Deng, W. Xue, R. Wang, H. Yi, C. Liu, Crit. Rev. Biotechnol. 38 (5) (2018) 671.
[34] B. Xia, T. Wang, X. Jiang, T. Zhang, J. Li, W. Xiao, P. Xi, D. Gao, D. Xue, J. Ding, ACS Energy Lett. 3 (2018) 2167.
[35] D. Huang, X. Gong, Y. Liu, G. Zeng, C. Lai, H. Bashir, L. Zhou, D. Wang, P. Xu, M. Cheng, J. Wan, Planta 245 (2017) 863.
[36] D. Huang, X. Wang, C. Zhang, G. Zeng, Z. Peng, J. Zhou, M. Cheng, R. Wang, Z. Hu, X. Qin, Chemosphere 186 (2017) 414.
[37] Z. He, F. Mansfeld, Sci. 2 (2009) 215.
[38] D. Huang, Y. Wang, C. Zhang, G. Zeng, C. Lai, J. Wan, L. Qin, Y. Zeng, RSC Adv. 6 (77) (2016) 73186.
[39] C. Zhang, C. Lai, G. Zeng, D. Huang, L. Tang, C. Yang, Y. Zhou, L. Qin, M. Cheng, Biosens. Bioelectron. 81 (2016) 61.
[40] B.Y. Chang, S.M. Park, Ann. Rev. Anal Chem. 3 (2011) 207.
[41] D. Huang, Z. Tang, Z. Peng, C. Lai, G. Zeng, C. Zhang, P. Xu, M. Cheng, J. Wan, R. Wang, J. Taiwan Inst. Chem. E. 77 (2017) 113.
[42] D. Huang, J. Li, G. Zeng, W. Xue, S. Chen, Z. Li, R. Deng, Y. Yang, M. Cheng, Chem. Eng. J. 375 (2019) 1.
[43] D. Huang, X. Yan, M. Yan, G. Zeng, C. Zhou, J. Wan, M. Cheng, W. Xue, A.C.S. Appl, Mater. Interfaces 10 (25) (2018) 21035.
[44] D. Huang, Z. Li, G. Zeng, C. Zhou, W. Xue, X. Gong, X. Yan, S. Chen, W. Wang, M. Cheng, Appl. Catal. B-Environ. 240 (2019) 153.
[45] Y. Luo, X. Li, X. Cai, X. Zou, F. Kang, H.M. Cheng, B. Liu, ACS Nano 12 (2018) 4565.
[46] H. Zhu, G. Gao, M. Du, J. Zhou, K. Wang, W. Wu, X. Chen, Y. Li, P. Ma, W. Dong, Adv. Mater. 30 (2018) 1707301.
[47] C. Tan, Z. Luo, A. Chaturvedi, Y. Cai, Y. Du, Y. Gong, Y. Huang, Z. Lai, X. Zhang, L. Zheng, Adv. Mater. 30 (2018) 1705509.
[48] Y.C. Chen, A.Y. Lu, P. Lu, X. Yang, C.M. Jiang, M. Mariano, B. Kaehr, O. Lin, A. Taylor, I.D. Sharp, L.J. Li, S.S. Chou, V. Tung, Adv. Mater. 29 (2017).
[49] H. Zhang, L. Yu, T. Chen, W. Zhou, X.W. Lou, Adv. Funct. Mater. 28 (2018).
[50] X. Shang, W.H. Hu, X. Li, B. Dong, Y.R. Liu, G.Q. Han, Y.M. Chai, C.G. Liu, Electrochim. Acta 224 (2017) 25.
[51] M.R. Gao, M.K.Y. Chan, Y. Sun, Nat. Commun. 6 (2015) 7493.
[52] J. Deng, H. Li, S. Wang, D. Ding, M. Chen, C. Liu, Z. Tian, K.S. Novoselov, C. Ma, D. Deng, Nat. Commun. 8 (2017) 14430.
[53] E.E. Benson, H. Zhang, S.A. Schuman, S.U. Nanayakkara, N.D. Bronstein, S. Ferrere, J.L. Blackburn, E.M. Miller, J. Am. Chem. Soc. 140 (2017).
[54] S.A. Shah, G. Zhu, X. Shen, L. Kong, Z.J, K. Xu, H. Zhou, J. Zhu, P. Song, C. Song, A. Yuan, X. Miao, Adv. Mater. Interfaces 7 (2018) 1801093.
[55] Z. Wu, J. Wang, R. Liu, K. Xia, C. Xuan, J. Guo, W. Lei, D. Wang, Nano Energy 32 (2017) 511.
[56] D. Huang, H. Luo, C. Zhang, G. Zeng, C. Lai, M. Cheng, R. Wang, R. Deng, W. Xue, X. Gong, X. Guo, T. Li, Chem. Eng J. 361 (2019) 353.
[57] G. Li, D. Zhang, Q. Qiao, Y. Yu, D. Peterson, A. Zafar, R. Kumar, S. Curtarolo, F. Hunte, S. Shannon, J. Am. Chem. Soc. 138 (2016) 16632.
[58] J. Xie, J. Zhang, S. Li, F. Grote, X. Zhang, H. Zhang, R. Wang, Y. Lei, B. Pan, Y. Xie, J. Am. Chem. Soc. 135 (2013) 17881.
[59] D. Huang, S. Chen, G. Zeng, X. Gong, C. Zhou, M. Cheng, W. Xue, X. Yan, J. Li, Coordin. Chem. Rev. 385 (2019) 44.
[60] G. Li, D. Zhang, Y. Yu, S. Huang, W. Yang, L. Cao, J. Am. Chem. Soc. 139 (2017) 16194.
[61] K.K. Paul, N. Sreekanth, R.K. Biroju, A.J. Pattison, D. Escalera-Lopez, A. Guha, T. N. Narayanan, N.V. Rees, W. Theis, P.K. Giri, J. Mater. Chem. A 6 (2018) 22681.
[62] Y. Liu, K. Wu, X.L. Guo, W.Y. Wang, Y.Q.A. Yang, J. Fuel Chem. Technol. 46 (2018) 535.
[63] T. Zhang, H. Zhang, Y. Ji, N. Chi, Y. Cong, Electrochim. Acta 285 (2018) 230.
[64] Y. Yi, B. Zhang, X. Jin, L. Wang, C.T. Williams, G. Xiong, D. Su, C. Liang, J. Mol. Catal. A-Chem. 351 (2011) 120.
[65] H.J. Kim, D. Kim, S. Jung, M.H. Bae, Y.J. Yun, S.N. Yi, J.S. Yu, J.H. Kim, D.H. Ha, J. Raman Spectrosc. 49 (2018) 1938.
[66] D. Huang, C. Liu, C. Zhang, R. Deng, R. Wang, W. Xue, H. Luo, G. Zeng, Q. Zhang, X. Guo, Bioresource Technol. 276 (2019) 127.
[67] C. Zhang, C. Lai, G. Zeng, D. Huang, C. Yang, Y. Wang, Y. Zhou, M. Cheng, Water Res. 95 (2016) 103.
[68] M.D. Siao, W.C. Shen, R.S. Chen, Z.W. Chang, M.C. Shih, Y.P. Chiu, C.M. Cheng, Nat. Commun. 9 (2018) 1442.
[69] K.K. Paul, L.P.L. Mawlong, P.K. Giri, ACS Appl. Mater. Interfaces 10 (2018) 42812.
[70] R. Ni, Y. Wang, X. Wei, J. Chen, P. Xu, W. Xu, J. Meng, Y. Zhou, Anal. Chim. Acta 1054 (2019) 47.
[71] A.D. Vogt, T. Han, T.P.B. Jr, Langmuir 13 (1997) 3397.
[72] W. Xue, Z. Peng, D. Huang, G. Zeng, J. Wan, R. Xu, M. Cheng, C. Zhang, D. Jiang, Z. Hu, J. Hazard. Mater. 359 (2018) 290.
[73] L. Gu, P. Ke, Y. Zou, X. Li, A. Wang, Appl. Surf. Sci. 331 (2015) 66.
[74] K. Tao, Y. Gong, J. Lin, Electrochim. Acta 274 (2018) 74.
[75] W. Wu, C. Niu, C. Wei, Y. Jia, C. Li, Q. Xu, Angew. Chem. Int. Ed. 58 (2019) 2029.
[76] C. Wang, T. Wang, J. Liu, Y. Zhou, D. Yu, J.K. Cheng, F. Han, Q. Li, J. Chen, Y. Huang, Energy Environ. Sci. 11 (2018) 2467.
[77] J. Fu, C. Bie, B. Cheng, C. Jiang, J. Yu, ACS Sustain. Chem. Eng. 6 (2018) 2767.
[78] Y. Cai, G. Zhang, Y. Zhang, J. Am. Chem. Soc. 136 (2014) 6269.